Check for updates

ADVANCED FUNCTIONAL MATERIALS
www.afm-journal.de

Mixed-Dimensional All-Organic Polymer Heterostructures with Enhanced Piezoelectricity

Wangwei Lian, Leiyang Wang, Jie Wang, Tao Cheng, Kun Dai, Bo Lu, Chuntai Liu, Caofeng Pan,* and Changyu Shen*

Enhancing the piezoelectricity of polymers while maintaining all components organic is still challenging but significantly important for developing flexible wearable energy harvesters and self-powered devices. Here, a novel and versatile strategy is introduced to construct mixed-dimensional all-organic polymer heterostructures (MPHs) for enhanced piezoelectricity. By combining all-polymer 1D nanofibers (NFs) with 2D crystals through epitaxial crystallization-driven assembly (ECA), MPHs are engineered to capitalize on the synergistic effects of both dimensional nanostructures. The intrinsic piezoelectric activity of 1D NFs is amplified by the growth of 2D crystals, enhancing force-sensitivity and overall piezoelectricity. The mixed-dimensional assembly not only enables controlled in-situ growth of MPHs, but also simultaneously induces preferential formation of electroactive phases through solvent-induced phase transition. By modulating the epitaxial growth of 2D crystals on 1D NFs, effective tuning of MPH growth amount and morphology is achieved, resulting in significant improvements in deformability, dipole polarization, and durability. MPHs exhibit remarkable piezoelectric improvements, achieving higher output under lower-level forces with a record-high sensitivity of ≈670 mV kPa^{-1}. Their superior responsivity enables the development of self-powered wireless wearable motion-monitoring systems for real-time physiological movement detection and analysis. This work inspires the development of all-organic piezoelectric devices for innovative flexible energy-harvesting and sensing applications.

1. Introduction

The increased global energy crisis and environment concerns have led to an urgent need for sustainable and clean energy sources. Piezoelectric materials have shown great promise in generating energy through mechanical-to-electrical conversion from the surrounding environment, such as human motions,[1] vibrations,[2] wind,[3] and sound waves.[4] With the rise of wearable, portable and implantable "battery-free" self-powered devices, there is a growing emphasis on flexible and lightweight piezoelectric materials.[5] Although inorganic counterparts like barium titanate ($BaTiO_3$),[6] zinc oxide (ZnO),[7] and lead zirconate titanate (PZT)[8] exhibit high piezoelectricity, their brittleness, toxicity, and processing difficulties limit their applications in flexible electronics. By contrast, organic piezoelectric polymers, including poly(vinylidene fluoride) (PVDF),[9] odd nylons,[10] cellulose[11] and poly(lactic acid),[12] are particularly attractive due to their superior flexibility, lightweight nature, biocompatibility, low cost, and ease of shaping. However, intrinsic piezoelectric polymers generate lower electric outputs than inorganic counterparts, posing a significant challenge.[13] Strategies to enhance polymer piezoelectricity often involve incorporating inorganic fillers, inevitably sacrificing flexibility and lightweight characteristics.[14] To meet the demands of miniaturized and wearable energy harvesting electronics, developing all-organic piezoelectric polymers with high performance, while preserving flexibility, lightweight, and robustness is of huge importance.

Considerable effort has been devoted to enhancing polymer piezoelectricity for increased electrical outputs. Common strategies include the electric poling,[15] mechanical stretching,[16] thermal annealing,[17] nanofiller incorporation,[18] and chemical synthesis.[19] These approaches induce dipole alignment and/or electroactive crystal nucleation, enhancing electrical generation in polymeric materials.[20] However, strict processing conditions and additives, such as high temperature, high-voltage poling field, and rigid inorganic fillers, are generally utilized, limiting large-scale manufacturing and applications.[21] Furthermore, these piezoelectric enhancements often compromise flexibility,

W. Lian, L. Wang, J. Wang, T. Cheng, K. Dai, B. Lu, C. Liu, C. Shen
State Key Laboratory of Structural Analysis, Optimization and CAE Software for Industrial Equipment, National Engineering Research Center for Advanced Polymer Processing Technology
Zhengzhou University
Zhengzhou 450002, China
E-mail: bolu@zzu.edu.cn
C. Pan
Institute of Atomic Manufacturing
Beihang University
Beijing 100191, China
E-mail: cfpan@binn.cas.cn

The ORCID identification number(s) for the author(s) of this article can be found under https://doi.org/10.1002/adfm.202404403

DOI: 10.1002/adfm.202404403

 © 2024 Wiley-VCH GmbH

increase cost, and introduce toxicity, unfavorable for developing wearable, eco-friendly, and cost-effective energy harvesting and sensing devices.

Geometric microengineering on existing piezoelectric polymers has opened avenues for enhanced electricity generation, due to its efficiency to increase piezo-potentials in response to mechanical stimuli.[22] In principle, piezoelectric output potential is directly proportional to the strain generated in materials according to: $V = d_{33}E\epsilon h/K$, where d_{33} is piezoelectric coefficient, E is the elastic modulus, ϵ is the strain, h is the material thickness, and K is the dielectric constant.[23] Accordingly, unique geometric structures sensitive to mechanical forces can maximize strain deformation and dipole polarization, boosting piezoelectric outputs with remarkable sensitivity.[24] Various geometric structures, such as pyramids,[25] micropillars,[26] and porous structures,[27] have been constructed on intrinsic piezoelectric polymers. However, the implications of these polymer structures are typically achieved through the utilization of special templates, chemical etching, and foaming, complicating device fabrication and limiting versatility and scalability. More importantly, previous microstructural designs predominantly focus on manipulating macroscopic geometry and surface features. A simultaneous control over microstructures down to the micro- and nanoscale, such as electroactive crystallization and molecular alignment, is always neglected. In fact, piezoelectric polymers are generally crystalline materials, whose piezoelectricity inherently depend on micro/nanoscale deformation and dipole polarizations within crystalline structures present.[28] Typically, most piezoelectric polymers such as PVDF and odd nylons are characterized by various crystalline phases (i.e., polymorphism), where only polar phases show the piezoelectricity effects due to higher dipolar moment.[29] Modulating the microscopic structures is by no means negligible. Therefore, an unconventional, general, and cost-effective route is highly desirable to simultaneously control both macro- and microscopic polymer structures toward developing all-organic piezoelectric polymeric energy harvesters.

Herein, we propose a mixed-dimensional assembly strategy to prepare a kind of all-organic piezoelectric polymer heterostructures. This design is based on two model polymers: nylon-11, a bio-based polymer selected as the piezoelectric matrix for its decent ferroelectricity, easy synthesis and non-toxicity compared to traditional PVDF, and polycaprolactone (PCL), a biodegradable polymer employed for its excellent crystallization properties.[30] The resulting mixed-dimensional all-organic polymer heterostructures (MPHs) consist of 1D nylon-11 nanofibers (NFs) and 2D PCL crystals, which are directly prepared through an epitaxial crystallization-driven assembly (ECA). The ECA process not only allows for the controllable growth of highly force-sensitive MPH architectures, but also simultaneously promotes the formation of electroactive crystals. By epitaxially growing 2D polymer crystals on 1D NFs, the resulting MPHs exhibit enlarged deformability and dipole polarizations under external stress, thereby promoting piezoelectric outputs with higher sensitivity. The piezoelectricity of MPHs is further tunable by modulating morphological evolutions. Additionally, the crosslinking effect of 2D crystals on 1D NFs via interfacial interactions leads to an interlocked nanofibril network within MPHs, rendering mechanical robustness, stabilization, and flexibility. MPH-based devices exhibit superior performance in energy harvesting and self-powered wireless detection of subtle physiological motions, demonstrating strong application potential in wearable and portable electronics for the electrical Internet of Things. Our mixed-dimensional assembly strategy is broadly applicable, which offers a general toolbox for designing all-organic polymeric piezoelectric devices with high performance. This approach can be extended to other piezoelectric polymers beyond the model polymers used in this study, thereby opening new avenues for the development of next-generation piezoelectric energy harvesting devices.

2. Results and Discussion

2.1. Mixed-Dimensional Assembly of MPHs

Piezoelectricity in our as-grown 1D/2D MPHs based on nylon-11 is achieved through the ECA process, without the need for additional stretching or high-voltage poling. The design of this novel piezoelectric all-polymer nanostructure was inspired by the force-sensitive leaves of Pterocarya stenopter, commonly known as Chinese wingnut (**Figure 1a**). The unique morphology of these leaves, characterized by 1D branches surface-grown with 2D disked leaves, allows for smart responsiveness to mechanical stimuli such as vibration, and wind in the environment. The ECA process not only realizes the controllable in-situ growth of force-sensitive all-polymer piezoelectric heterostructures, but also allows simultaneous control over polar crystal phases crucial for piezoelectricity. The resulting all-organic polymer heterostructures exhibit significantly amplified piezoelectricity, rendering them suitable for both mechanical energy harvesting and self-powered smart stimuli-sensing applications. This approach offers a straightforward and versatile approach to fabricating all-organic polymeric piezoelectric materials, promising for use in smart wearable and portable piezoelectric devices (Figure 1b).

The fabrication strategy of MPHs is schematically illustrated in Figure 1c. First, 1D aligned NFs of nylon-11 is obtained through electrospinning. Subsequently, these NFs are surface-doped by 2D lamellar polymer crystals growing in situ through the ECA process, utilizing a model crystallizable polymer, PCL. Specifically, the nascent nylon-11 NFs are incubated in the PCL/Acetic acid (AcOH) doping polymer solution at room temperature, enabling the direct growth of 2D PCL crystals on fiber surfaces to assembly these materials with different dimensionalities into mixed-dimensional heterostructures. Owing to favorable intermolecular interactions at nylon-11/PCL interface, the 1D NFs with the larger specific area provide abundant nucleating sites for the epitaxial crystallization of PCL, facilitating the in-situ growth of MPHs. To ensure epitaxial growth and minimize homogeneous nucleation, the concentration of doping polymer solutions (c) is carefully controlled within unentangled regimes, specifically around the critical overlap concentration c^* (≈0.43 wt% for PCL). Beyond this threshold ($c \gg c^*$), polymer chains would overlap and entangle, reducing their mobility and leading to homogeneous nucleation within the bulk solution rather than at the nanofiber surfaces. More interestingly, the ECA process simultaneously induces enhanced formation of piezoelectric crystals (i.e., polar δ'-phase) inside nylon-11 NFs. The molecular origin is revealed to be the phase transition from α- to δ'-phase induced by AcOH solvent through protonation effect (Figure 1c). As an

© 2024 Wiley-VCH GmbH

16163028, 0, Downloaded from https://onlinelibrary.wiley.com/doi/10.1002/adfm.202404403 by Cas-Beijing Institution Of, Wiley Online Library on [30/06/2024]. See the Terms and Conditions (https://onlinelibrary.wiley.com/terms-and-conditions) on Wiley Online Library for rules of use; OA articles are governed by the applicable Creative Commons License

16163028, 0, Downloaded from https://onlinelibrary.wiley.com/doi/10.1002/adfm.202404403 by Cas-Beijing Institution Of, Wiley Online Library on [30/06/2024]. See the Terms and Conditions (https://onlinelibrary.wiley.com/terms-and-conditions) on Wiley Online Library for rules of use; OA articles are governed by the applicable Creative Commons License

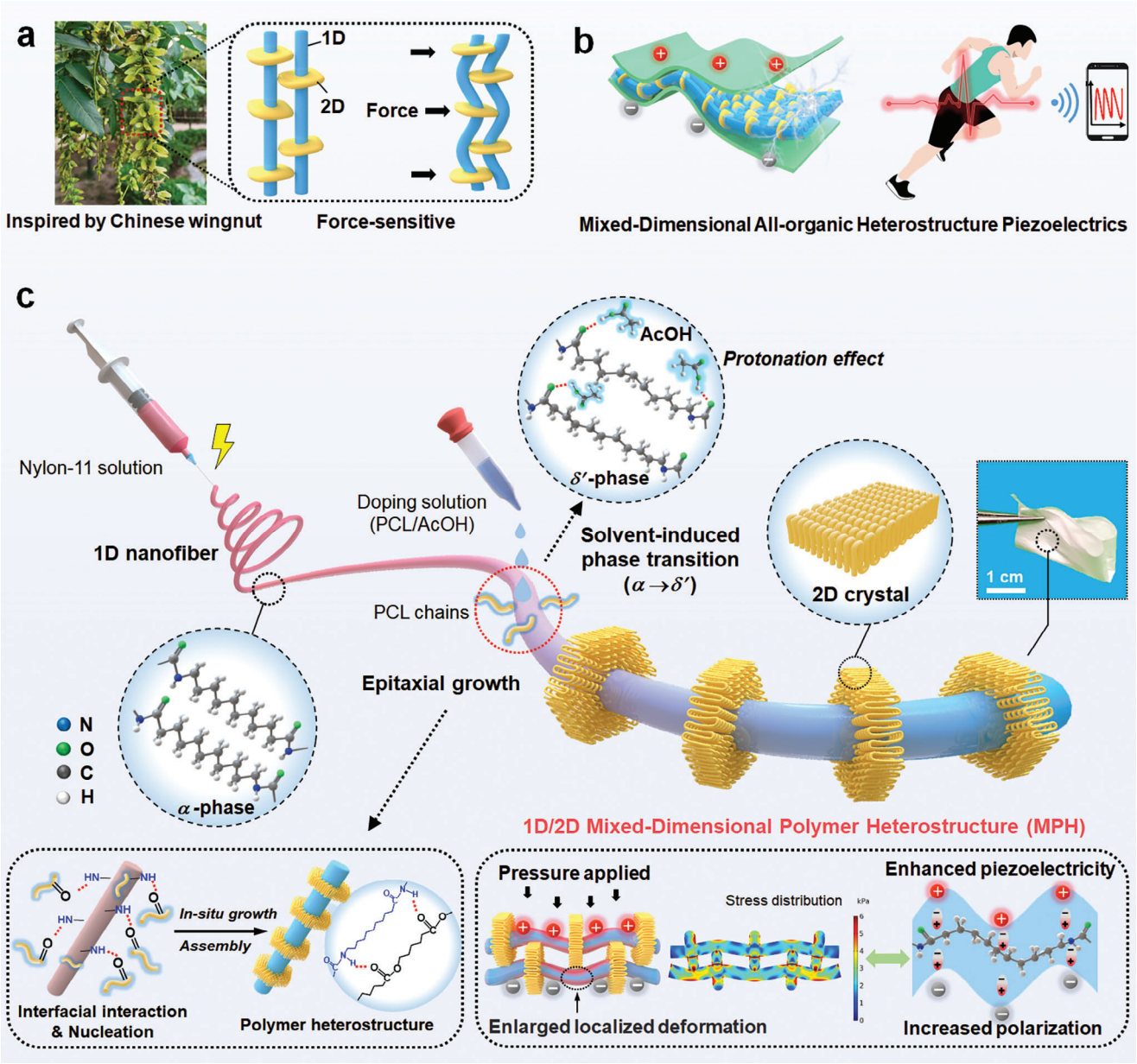

Figure 1. Mixed-dimensional structure design and fabrication of MPHs. a) Photographs showing the typical force-sensitive structure of Chinese wingnut leaves. b) Schematic of bioinspired flexible all-organic piezoelectric electronics composed of 1D/2D MPHs. c) Schematic illustration of the assembly process and mechanisms of MPHs based on nylon-11@PCL hybrids. Inset in the bottom left corner illustrates the in-situ growth of 2D PCL crystals on 1D nylon-11 NFs during ECA process. Inset in the bottom right corner depicts the piezoelectric enhancement mechanism of MPHs.

outcome, MPHs based on nylon-11 with preferable piezoelectric crystals are obtained in a single step. It is also noteworthy that the presence of epitaxial 2D crystals in such heterostructures links adjacent 1D NFs to form a well-defined interlocked nanofibril network, which not only stabilizes the nanofibrous structure, but also renders mechanical robustness with sufficient flexibility. The resulting MPH membranes are freestanding, flexible and lightweight with a density of ≈0.41 g cm^{-3} (Figure 1c), showing significant potential in wearable energy harvesters and sensors. Due to the enlarged strain-potential effects by the unique structure, MPHs exhibit improved deformability and dipole polarizations in response to external stresses, resulting in an enhanced piezoelectricity (Figure 1c).

The growth mechanism was elucidated through morphology studies of MPHs fabricated by varying the concentration of doping polymer solutions. Original nylon-11 NFs exhibit smooth surfaces with an average diameter of 270 ± 62 nm (**Figure 2a**). Upon immersion in PCL/AcOH solution, periodic 2D lamellar crystals grow on fiber surfaces along the longitudinal direction, comprising folded PCL molecular chains. To facilitate clear observations, excess uncrystallized PCL regions were selectively extracted by the fresh solvent of AcOH/deionized water (1/1, v/v).

 © 2024 Wiley-VCH GmbH

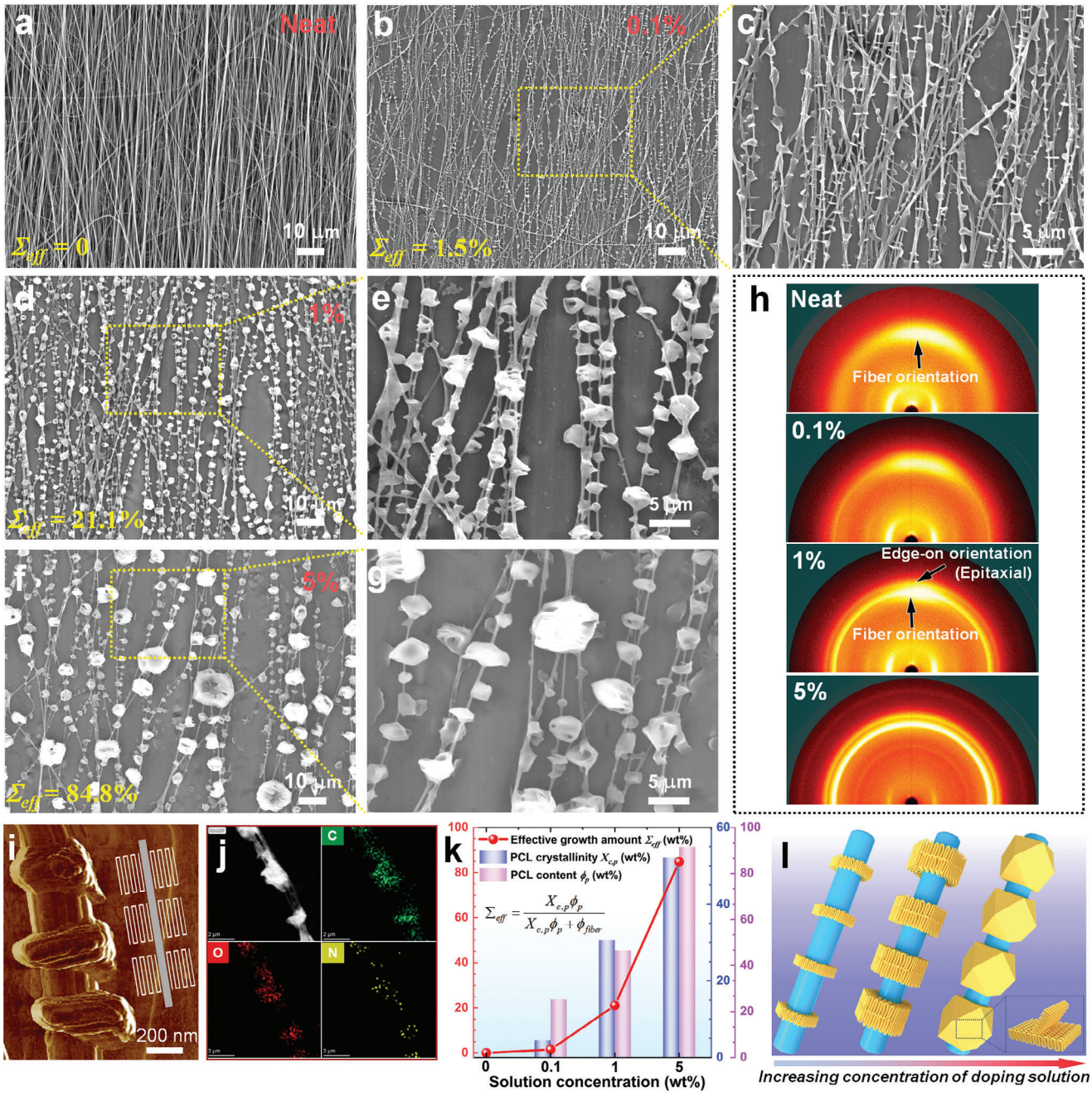

Figure 2. Effects of doping polymer solution on morphology development of MPHs. SEM images of MPHs fabricated with different concentrations of PCL doping solution: a) neat nylon-11 NFs, b) 0.1 wt%, d) 1.0 wt% and f) 5.0 wt%. c,e,g) are enlarged images of b,d,f), respectively. Note that uncrystallized PCL regions in MPHs had been extracted for microscope observations. h) 2D-WAXD patterns of MPHs prepared with varying concentration of doping polymer solutions. i) AFM height images of MPHs. j) TEM and EDS element mapping images of MPHs. k) Dependences of the effective growth amount (Σ_{eff}), weight fraction and crystallinity of PCL in MPHs as a function of the concentration of doping polymer solutions. l) Dependence of morphology evolutions of MPHs on the concentration of doping polymer solutions.

SEM images of the resulting hybrid NFs reveal the formation of the unique mixed-dimensional heterostructure, featuring 1D nylon-11 NFs doped by periodic 2D PCL crystals with edge-on orientation along the out-of-plane direction (Figure 2b–g). Cross-sectional SEM images of the entire nanocomposite confirm the widespread occurrence of this unique heterostructure throughout the membranes (Figure S1, Supporting Information). The edge-on orientation of epitaxial crystals is evidenced by strong $(100)_{PCL}$ diffraction arcs on the meridian of WAXD patterns (Figure 2h). The formation of MPHs is further visualized by AFM and TEM micrographs (Figure 2i–j). It is worth noting that the morphology of MPHs exhibits a strong dependence on the

© 2024 Wiley-VCH GmbH

16163028, 0, Downloaded from https://onlinelibrary.wiley.com/doi/10.1002/adfm.202404403 by Cas-Beijing Institution Of, Wiley Online Library on [30/06/2024]. See the Terms and Conditions (https://onlinelibrary.wiley.com/terms-and-conditions) on Wiley Online Library for rules of use; OA articles are governed by the applicable Creative Commons License

concentration of doping polymer solutions (Figure 2b–g). At lower solution concentrations ($c/c^* < 1$), epitaxial crystals are smaller due to the limited amount of polymer chains in the dilute solution (Figure 2b,c). With an increase in concentration ($c/c^* > 1$), crystal sizes remarkably increase, indicating enhanced epitaxial growth (Figure 2d,e). Specifically, crystal diameters increase from 730 ± 20 nm to 3.06 ± 1.02 µm as the solution concentration increases from 0.1 to 5 wt%. Moreover, at higher concentrations ($c/c^* \sim 10$), globular crystals with larger diameters appear on fiber surfaces (Figure 2f,g). This observation is ascribed to the surface-induced crystal growth in semidilute solutions: periodic lamellar crystals initially form on fiber surfaces, and then the remaining polymer chains in the solution crystallize on the surface of preformed crystals that act as new nucleation sites. The morphology evolution of MPHs is further confirmed by WAXD (Figure 2h). For lower concentrations, insensitive meridian $(100)_{PCL}$ reflections of MPHs, compared to the original NFs, indicate the formation of 2D crystals comprising folded molecular chains with *c*-axis parallel to the longitudinal direction of fibers. Whereas, at higher concentrations, dispersed WAXD patterns are observed due to additional crystal growth perpendicular to the surface of existing 2D crystals, resulting in a decrease in overall detected crystal orientation. Further increasing the concentration well beyond c^* (i.e., $c \gg c^*$, concentrated solutions) results in dominant homogeneous nucleation and crystallization (i.e., spherulites) in the bulk due to increased chain–chain entanglements, which are unfavorable for MPH formation (Figure S2, Supporting Information). Therefore, this work primarily focuses on the preferential formation of MPHs in doping polymer solutions within dilute and semidilute regimes ($0.1 < c/c^* < 10$).

To quantify the actual amount of epitaxial crystals growing on NFs, the MPH membranes were subjected to melting via DSC. Based on the difference between melting behaviors of two components ($T_m \approx 190$ °C for nylon-11 versus $T_m \approx 58$ °C for PCL, Figure S3, Supporting Information), the effective growth amount of crystals (Σ_{eff}) on the surface of NFs was determined (Table S1, Supporting Information). Specifically, Σ_{eff} for MPHs was computed using a proposed equation (see derivation details in Note S1, Supporting Information):

$$\sum_{eff} = \frac{X_{c,p}\phi_p}{X_{c,p}\phi_p + \phi_{fiber}} \tag{1}$$

where ϕ_p and ϕ_{fiber} are the weight fraction of components PCL and nylon-11 NFs in MPH membranes, respectively; and $X_{c,p}$ denotes the total crystallinity of PCL in membranes, encompassing both epitaxial and bulk crystallizations. Specifically, Σ_{eff}, indicative of epitaxial PCL crystallinity on fiber surfaces, is increased from 1.5 wt% to 84.8 wt% with an increase in the doping solution concentration from 0.1 wt% to 5.0 wt% (Figure 2k). This observation suggests an enhanced coverage of 2D crystals on the surface of NFs, consistent with SEM observations. The enhanced epitaxial crystal growth also increases the total crystallinity of PCL in the membranes with $X_{c,p}$ increasing from 4.5% to 52.2%. The observed enhancement in epitaxial crystal growth on NFs with increasing doping solution concentration is attributed to the augmented number of polymer chains available for crystallization, thereby improving crystallite perfection. However, further increases in concentration ($c \gg c^*$) could enhance the total crystallinity of PCL but diminish its epitaxial crystallization on fiber surfaces (lower Σ_{eff}), as the homogeneous nucleation in the bulk begins to dominate crystallization over heterogeneous nucleation (Figure S2, Supporting Information). Morphological evolutions of MPHs depending on the concentration of doping polymer solutions are depicted by a proposed scheme in Figure 2l. These findings indicate the high tunability of the as-grown MPH morphology through the ECA strategy.

2.2. Molecular Mechanism and Microstructural Analyses of MPHs

To gain deeper insights into the molecular origin of MPHs, their chemical structure was examined using FTIR (**Figure 3**a). Noticeably, with an increase in the growth amount of PCL crystals, simultaneous blue shifts in the C = O bands of PCL (from 1721 to 1725 cm^{-1}) and red shifts in the N–H bands of nylon-11 (from 3305 to 3303 cm^{-1}) are observed, alongside shifts in the overlapped N–H bending and C–N stretching bands (from 1541 to 1543 cm^{-1}). These chemical shifts indicate the formation of hydrogen bonds (O···H–N) between components nylon-11 and PCL (Figure 3b). The intermolecular hydrogen-bonding interactions enhances the interfacial compatibility between the two materials, thereby promoting the heterogeneous nucleation and growth of epitaxial crystals in MPHs. According to the classical heterogeneous nucleation theory,[31] the formation of heterogeneous nucleus on substrate surfaces depends on the reduction in the free enthalpy of nucleation (ΔG^*) expressed by:

$$\Delta G^* = \frac{16\gamma\gamma_e\Delta\gamma T_m^{0\,2}}{\left(\Delta H_f \Delta T\right)^2} \tag{2}$$

where γ and γ_e represent the side and end surface free energies of crystals, respectively, $\Delta\gamma$ is the interfacial free energy difference, T_m^0 is the equilibrium melting temperature of crystals, ΔH_f is the enthalpy of fusion per unit volume of crystals, and ΔT is the supercooling degree. Consequently, the decrease in the interfacial free energy difference ($\Delta\gamma$) reduces the barrier for nucleation and enhances the growth of epitaxial crystals on 1D NFs within MPHs (Figure 3c). The presence of intermolecular H-bond interactions between nylon-11 and PCL significantly reduces the interfacial tension (free energy) and lowers the nucleation energy barrier, thereby facilitating the epitaxial growth of 2D crystals under mild conditions.

To explore further the presence of piezoelectric crystals in this unique heterostructure, the crystalline phases of MPHs were thoroughly examined. FTIR spectra reveals absorption bands at 689 cm^{-1} and 585 cm^{-1}, corresponding to α-phase of nylon-11 for all membranes (Figure 3a).[32] The exact crystal structures were further clarified through WAXD analysis (Figure 3d). In addition to α-phase diffractions, distinct diffraction peaks at $2\theta = 6.7°$ are observed in all membranes, which are exclusively attributed to the typical (001) planes of δ'-phase of nylon-11 (Table S2, Supporting Information).[32–33] Strong peaks in the 2θ range of 20–25° are associated with the overlapping diffractions of α(100) (20.4°), δ'(100) (21.4°), α(010)/(110) (22.9°) of nylon-11 and (110) (21.1°) and (200) (23.3°) planes of PCL.

© 2024 Wiley-VCH GmbH

16163028, 0, Downloaded from https://onlinelibrary.wiley.com/doi/10.1002/adfm.202404403 by Cas-Beijing Institution Of, Wiley Online Library on [30/06/2024]. See the Terms and Conditions (https://onlinelibrary.wiley.com/terms-and-conditions) on Wiley Online Library for rules of use; OA articles are governed by the applicable Creative Commons License

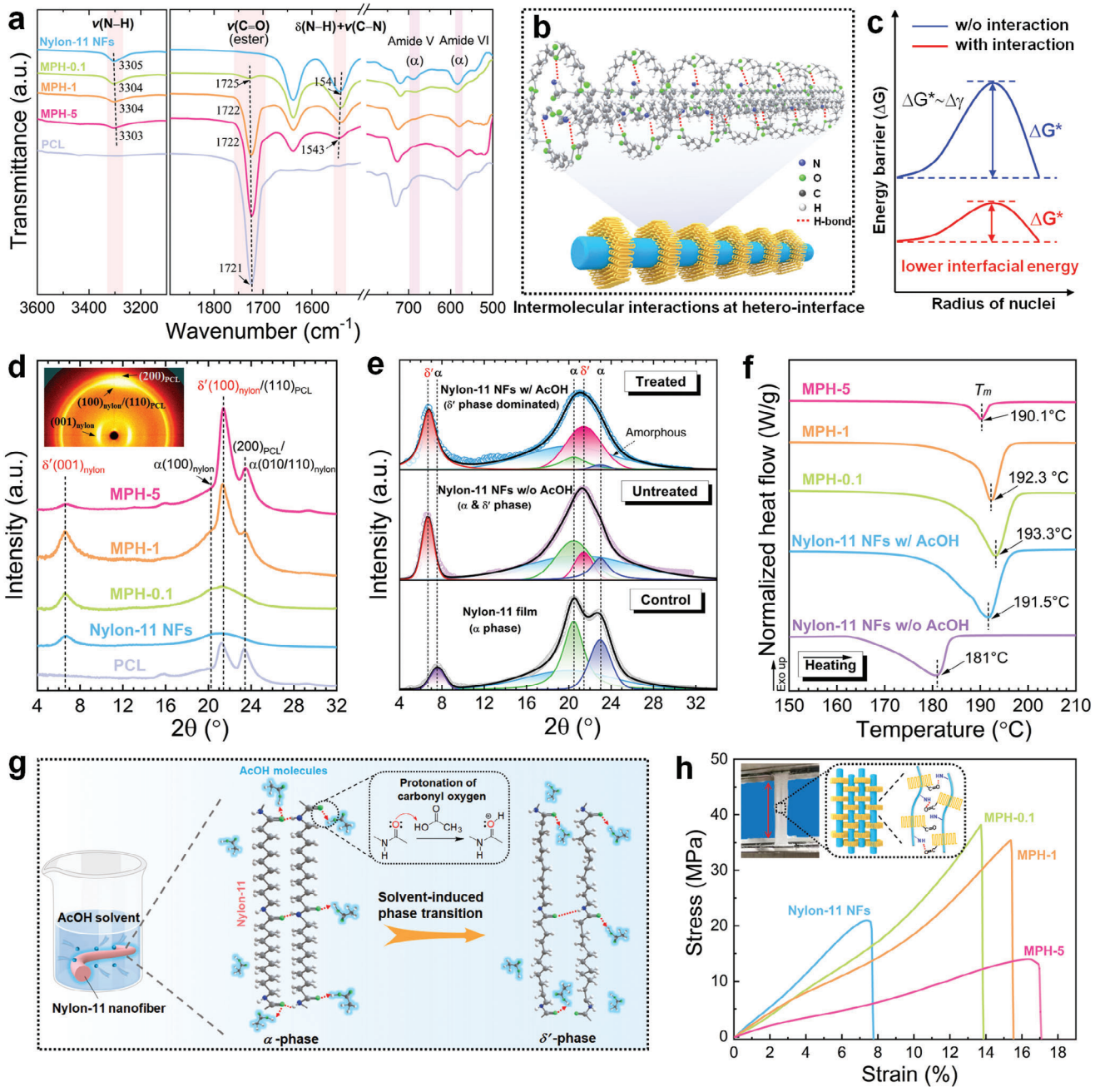

Figure 3. Molecular mechanism and microstructural analyses of MPHs. a) FTIR spectra of MPHs and control systems. b) Schematic diagram of intermolecular interactions between nylon-11 NFs and PCL crystals in MPHs. c) Schematic presentation indicating the energy barriers of heterogeneous crystallization with and without interfacial interactions. d) WAXD spectra of MPHs and control systems. e) Comparison of WAXD reflections for nylon-11 NFs treated with and without AcOH and control nylon-11 film. f) DSC thermographs of MPHs and control nylon-11 NFs. g) Schematic diagram of phase transition from α-phase to δ'-phase of nylon-11 induced by AcOH through protonation effect. h) Stress-strain curves of MPH membranes.

These findings confirm the presence of piezoelectric nylon δ'-phase crystals in MPHs. The existence of δ'-phase is attributed to two factors. First, the ultra-fast evaporation of trifluoroacetic acid (TFA)/1,1,1,3,3,3-hexafluoro-2-propanol (HFIP) mixed solvent during the electrospinning process induces the formation of δ'-phase characterized by a poorly organized hydrogen-bonded chain arrangement.[33b] Second, the AcOH solvent employed during the MPH assembly process further promotes the development of δ'-phase inside nylon-11 NFs. To validate this concern, we compared the WAXD profiles of nylon-11 NFs with and without AcOH treatment, and the reference nylon-11 films (pure α-phase) (Figure 3e). It is noteworthy that nylon-11 NFs treated with AcOH exhibit a broader diffraction peak in 2θ range of 20–25° compared to untreated nylon-11 NFs and reference films. Quantitative deconvolution analysis of diffraction peaks reveals an enhanced $\delta'(100)$ reflection in nylon-11 NFs treated with AcOH,

© 2024 Wiley-VCH GmbH

16163028, 0, Downloaded from https://onlinelibrary.wiley.com/doi/10.1002/adfm.202404403 by Cas-Beijing Institution Of, Wiley Online Library on [30/06/2024]. See the Terms and Conditions (https://onlinelibrary.wiley.com/terms-and-conditions) on Wiley Online Library for rules of use; OA articles are governed by the applicable Creative Commons License

with a higher relative fraction of δ'-phase of $K_{\delta'}$ ≈84.1% compared to untreated counterparts (≈40.2%) ($K_{\delta'} = A_{\delta'}/(A_{\delta'}+A_{\alpha}) = (A_{\delta'(001)}+A_{\delta'(100)})/(A_{\delta'(001)}+A_{\delta'(100)}+A_{\alpha(100)}+A_{\alpha(010)/(110)})$, A is integrated diffraction peak area) (Figure 3e). This promotion in δ'-phase crystallization is further validated by DSC analysis (Figure. 3f). Original nylon-11 NFs exhibits a lower melting point (T_m) of 181 °C originating from the α-phase fusion.[32] However, after AcOH treatment, the T_m is increased to a higher temperature of 191.5 °C that is consistent with the typical melting of δ'-phase.[32] Meanwhile, all MPH membranes containing nylon-11 NFs displays the higher T_m above 190 °C, indicating the dominance of δ'-phase crystallization. These findings underscore the critical role of AcOH in promoting the evolution of nylon-11 δ'-phase during the mixed-dimensional assembly.

The molecular mechanism underlying the promoted δ'-phase formation in MPHs is attributed to solvent-induced phase transition. To shed light upon the mechanism, we analyzed chemical structures of nylon-11 NFs with and without AcOH treatment using FTIR (Figure S4, Supporting Information). Evidently, upon treatment with AcOH, the C=O stretching band for amides of nylon-11, which is sensitive to the information of chain packing and hydrogen bonds between amide groups, is shifted slightly to higher wavenumbers (from 1637 to 1639 cm^{-1}). Similarly, the N–H stretching band shifts from 3303 to 3305 cm^{-1}. These notable shifts in amide bands to higher wavenumbers clearly indicate the formation of less ordered chain packing and H-bonds in nylon molecules.[29a,34] This is associated with the increased δ'-phase, which is a metastable crystal containing randomly organized H-bonds among chains, in agreement with WAXD results. This is due to the fact that when nylon-11 meets AcOH solvent, carbonyl oxygen atoms of amides are protonated with accompanying H-bonds weakening among nylon chains, as a result of strong interactions between amide groups and acid molecules (Figure 3g).[29a,35] Consequently, the chain conformation of nylon-11 shifts to a loosely packed state, facilitating the transformation of α-phase toward δ'-phase. This elucidates the promoted δ'-phase formation in MPHs achieved through the ECA process in PCL/AcOH solutions. Hence, the ECA process serves as a "kill two birds with one stone" strategy, achieving not only the assembly of polymeric 1D NFs and 2D crystals but also effectively inducing the preferential growth of electroactive δ'-phases for enhanced piezoelectricity.

It is also noteworthy that as-grown MPHs significantly enhance mechanical robustness while improving compressibility. Stress-strain curves reveals a substantial enhancement in both tensile strength and ductility in MPHs relative to original nylon-11 NFs (Figure 3h; Table S3, Supporting Information). Specifically, the MPH prepared at a doping solution concentration of 0.1 wt% exhibits a tensile strength of 41.9 ± 3.4 MPa and strain at break of 15.1 ± 1.8%, nearly twice as large as that of original NFs. Such enhancements arise from the physical crosslinking between adjacent 1D nylon-11 NFs facilitated by epitaxial 2D PCL crystals particularly in the presence of strong interfacial hydrogen-bonding interactions (see inset in Figure 3h). As verified by morphological results, the epitaxial growth of 2D crystals connects individual NFs to form a more stabilized interlocked nanofibrous network (Figure S1, Supporting Information), enhancing resistance to external deformations. MPHs demonstrate a broader linear viscoelastic region up to 2 MPa (Figure S5, Supporting Information), ensuring structural integrity without interfacial detachment, even under higher stress levels (50 kPa or more) characteristic of pressure ranges for mechanical energy harvesting applications. Moreover, MPH membranes show a decrease in tensile modulus compared to the original NFs, mainly due to the low modulus of surrounding PCL matrix and the presence of numerous inter-fiber voids (Figure S6, Supporting Information). This reduction in modulus improves compressibility and flexibility, consequently amplifying sensitivity to mechanical stimuli. MPHs exhibit superior ductility, manifesting in greater elongation at break compared to inorganic materials like ZnO (5%), albeit with lower mechanical strength. Moreover, elevating the doping solution concentration above 5.0 wt% diminishes tensile strength due to the formation of globular crystals with larger sizes.

2.3. Piezoelectric Properties and Mechanoelectrical Mechanisms of MPHs

To assess the enhanced piezoelectricity realized by the 1D/2D mixed-dimensional heterostructure, we conducted a comprehensive evaluation of the piezoelectric performance of MPHs under periodic compressive stress. **Figure** 4a illustrates the schematic of the piezoelectric device based on MPHs. The deformation was meticulously controlled within the linear viscoelastic regions with a force of 5 N (5.6 kPa) and pressing frequency set at 3 Hz. Alternating electric signals are generated from the device subjected to periodic pressing and releasing (Figure 4b). The amplitudes of output signals from MPHs in forward and reverse connection modes are nearly identical, as confirmed by a polarity switching test (Figure S7, Supporting Information), thereby affirming that the observed electrical signals originate from the piezoelectric effect, rather than external interference or other sources. Intriguingly, all MPH devices produce higher electrical outputs compared to pure nylon-11 NFs (Figure 4c). With an increase in the growth of epitaxial 2D polymer crystals, a gradual improvement in output performance is observed. For instance, MPH-5 exhibits the maximum output current of 0.5 μA and voltage of 3.4 V, approximately twice that of pure NFs (Figure 4c). The outputs generated at a low pressure (5.6 kPa) are clearly higher than these of other similar piezoelectric polymers, for instance, nylon-11 (0.01 V, 10 kPa)[21] and PVDF (0.25 V, 60 kPa)[36] (Table S4, Supporting Information). The piezoelectric enhancement is consistent with the increase in piezoelectric coefficient $|d_{33}|$ (Table S5). Pure nylon-11 NFs exhibits a $|d_{33}|$ of 5.8 ± 0.3 pC N^{-1}, whereas all MPHs show a significant increase. Notably, MPH-5 exhibits a maximum $|d_{33}|$ of 15.1 ± 0.2 pC N^{-1}, nearly 200% greater than that of pure nylon-11 NFs. The observed piezoelectric improvement is quite interesting, since PCL itself is not inherently a ferroelectric or piezoelectric polymer. Moreover, the δ'-phase promotion within nylon-11 NFs, induced by the assembly of MPHs, should be of the same level for all systems due to the identical fabrication conditions. Therefore, the enhancement in electric outputs originates primarily from the introduction of 2D crystals on 1D NFs in as-grown MPH architecture. To identify the critical role of epitaxial crystals in enhancing piezoelectricity, we selectively etched PCL crystals from the surface of nylon-11 NFs using fresh AcOH solvent (Figure 4d, SEM image of etched

© 2024 Wiley-VCH GmbH

16163028, 0, Downloaded from https://onlinelibrary.wiley.com/doi/10.1002/adfm.202404403 by Cas-Beijing Institution Of, Wiley Online Library on [30/06/2024]. See the Terms and Conditions (https://onlinelibrary.wiley.com/terms-and-conditions) on Wiley Online Library for rules of use; OA articles are governed by the applicable Creative Commons License

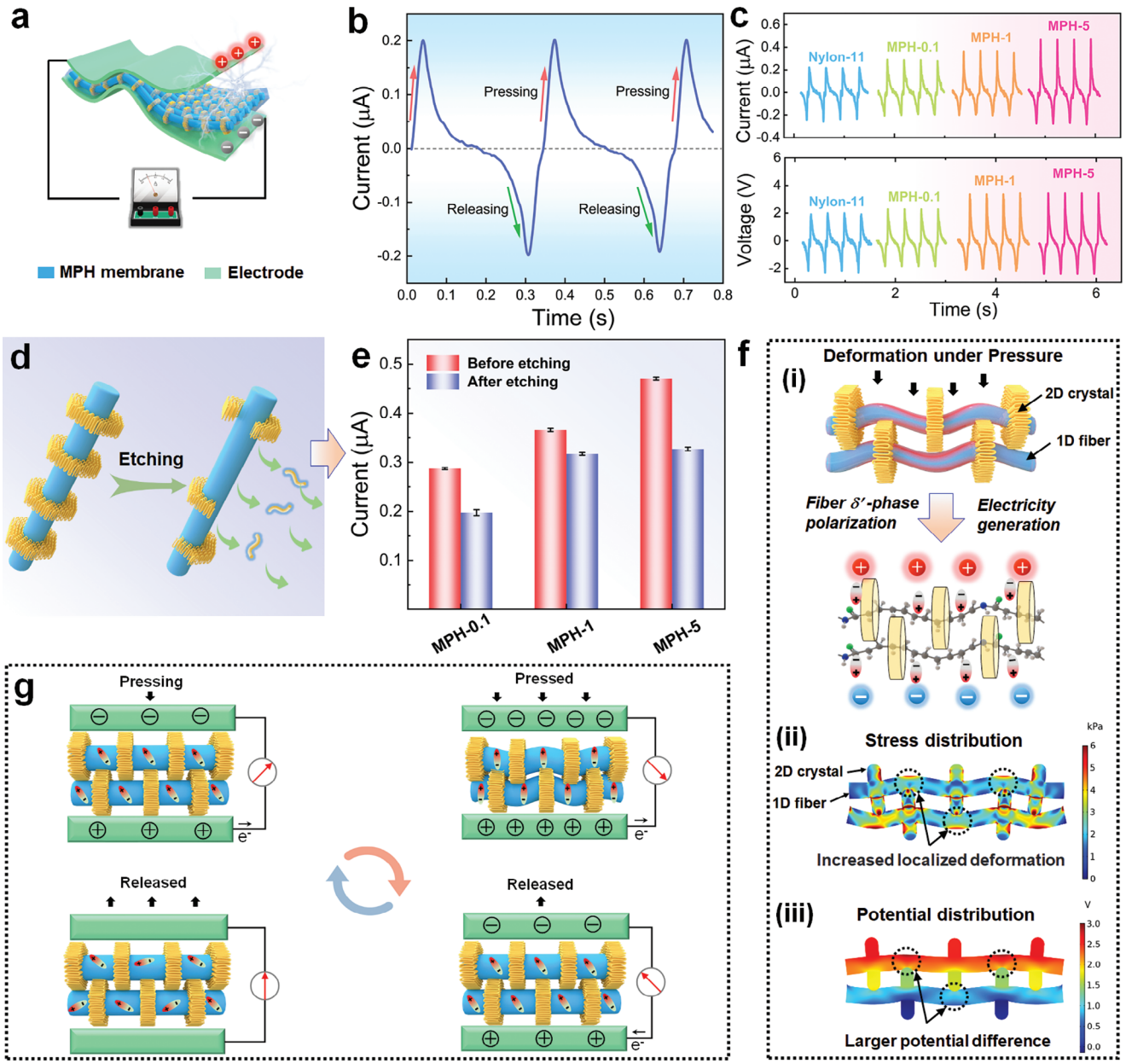

Figure 4. Piezoelectric properties and mechanisms of MPHs. a) Schematic illustration of MPH-based piezoelectric devices. b) Piezoelectric output current signals of MPHs subjected to periodic pressing/releasing. c) Piezoelectric output current and voltage of MPHs with varying loadings of epitaxial 2D crystals under a dynamic pressure of 5 N at 3 Hz. d) Schematic diagram showing the etching treatment of MPHs using AcOH solvent. e) Comparison of output current before and after etching for MPHs. f) Schematic illustration of the mechanoelectrical mechanism for piezoelectric effect of MPHs. Lower panels in (f) show the FEM simulation of stress and potential distributions of MPHs under a vertical pressure of 5 kPa. g) Schematic illustration showing the working principle for piezoelectric responses of MPHs under periodic pressing/releasing.

MPHs is shown in Figure S8, Supporting Information). After etching, the electrical outputs of all MPH devices are dramatically decreased (Figure 4e; Figure S9, Supporting Information), indicating the indispensable contribution of epitaxial crystals to the piezoelectric enhancement. The slightly larger electrical outputs for membranes with higher growth amount may be attributed to the presence of some surviving PCL crystals.

The significant improvement in piezoelectricity of MPHs is closely related to the enhanced microscopic deformation and dipole polarizations (Figure 4f(i)). To elucidate further the mechanoelectrical mechanism, we qualitatively analyzed the stress and electric potential distributions of MPHs under external forces through a finite-element-method (FEM) simulation using COMSOL Multiphysics software (see simulation parameters in Note S2, Supporting Information). Due to modulus disparity between component nanostructures with varying dimensions and sizes, the stress is more geometrically concentrated at heterostructure interfaces and transferred efficiently to

© 2024 Wiley-VCH GmbH

16163028, 0, Downloaded from https://onlinelibrary.wiley.com/doi/10.1002/adfm.202404403 by Cas-Beijing Institution Of, Wiley Online Library on [30/06/2024]. See the Terms and Conditions (https://onlinelibrary.wiley.com/terms-and-conditions) on Wiley Online Library for rules of use; OA articles are governed by the applicable Creative Commons License

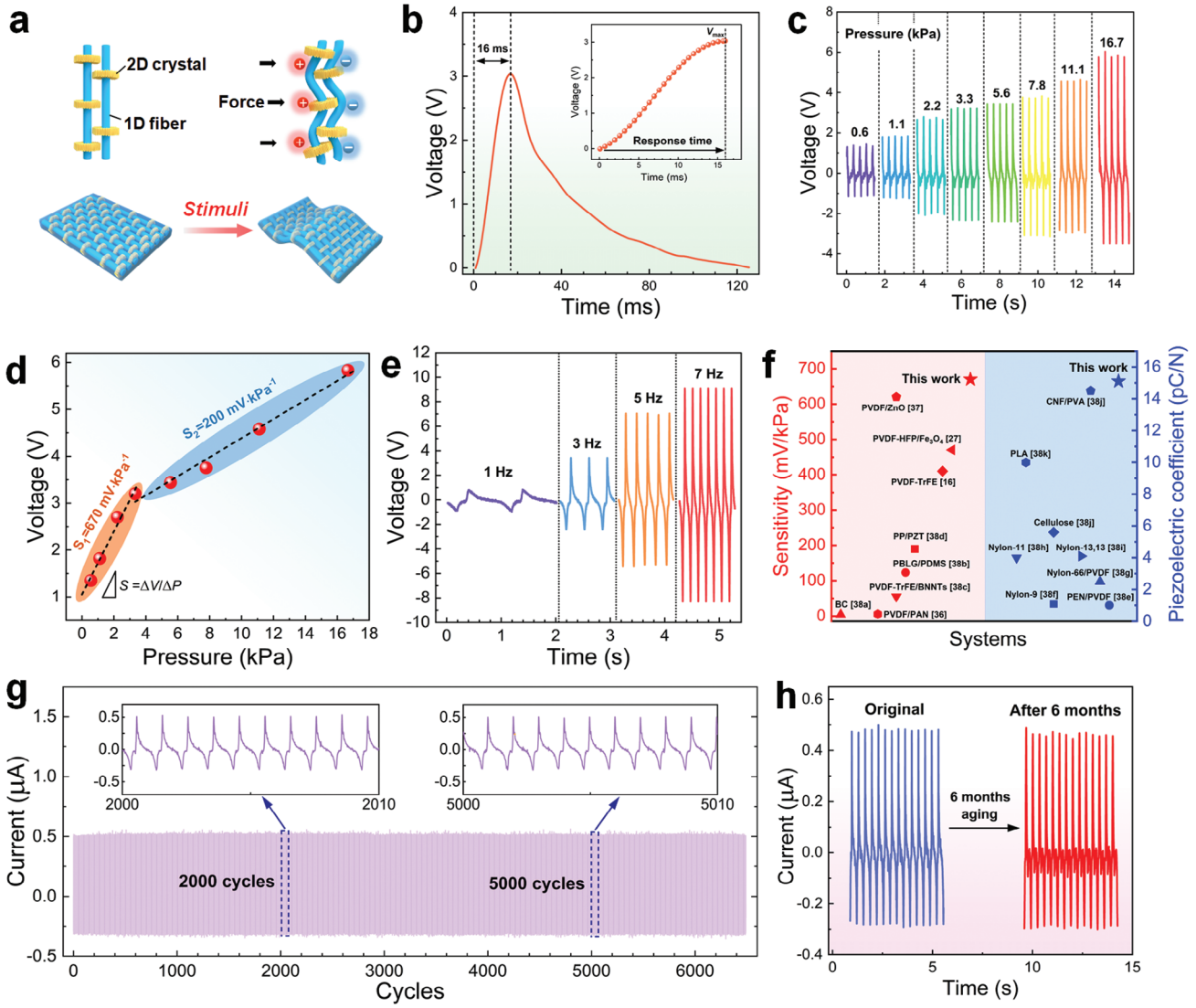

Figure 5. Electrical characteristics of MPHs. a) Schematic illustration of the force-sensitive behavior of MPHs under mechanical stimuli. b) Response time of MPHs. c) Pressure-dependent output voltage of MPHs. d) Sensitivity of MPHs in different ranges of pressure. e) Frequency-dependent output voltage of MPHs. f) Comparison of piezoelectric performances between MPHs and other polymeric piezoelectric systems. g) Stability evaluation of MPHs tested over 6000 cycles under a periodic force of 5 N at 3 Hz. h) Comparison of output current of MPHs before and after being stored for 6 months in the normal environment. Electrical characteristics of MPHs are representatively demonstrated based on the optimum MPH-5.

internal 1D NFs (Figure 4f(ii)). This leads to significant strain deformation of nylon-11 chains, inducing more effective polarization of δ'-phase dipoles and generating higher electric potential (Figure 4f(iii)). As such, a higher growth amount of epitaxial 2D crystals (Σ_{eff}) with larger crystallite sizes and perfection leads to greater piezoelectricity. In summary, the synergistic effect of the force-sensitive structure of MPHs and the presence of polar δ'-phase crystals leads to the substantial enhancement of piezoelectric outputs (Figure 4g). When MPHs experience compressive stresses, the structure is squeezed and the inter-fiber voids get contracted, such that the rigid 2D crystals squeeze the soft 1D NFs. As a result, nylon δ'-phase crystals within NFs are deformed, dipoles are polarized, and potential difference between two electrodes is created, driving the flow of electrons. Upon force removal, the potential difference vanishes, and the accumulated free charges flow back, resulting in a reverse current.

It is also noteworthy that MPHs are highly sensitive to the mechanical stimuli in the form of electrical signals (**Figure 5a**). Hereafter, the optimum MPH-5 is selected to represent the electrical characteristics among the tested MPHs. These devices exhibit an impressively short response time of 16 ms upon exposure to external stress stimuli (Figure 5b). Furthermore, MPHs a demonstrate particular sensitivity to changes in applied stress (Figure 5c). Figure 5d depicts the plot of output voltage as a function of pressures, which reveals two distinct linear response regions depending on pressure amplitudes. The sensitivity (S) was determined from the slope ($S = \Delta V/\Delta P$), where ΔV and ΔP represent voltage and pressure changes, respectively. MPHs displays a high sensitivity of 670 mV kPa^{-1} in the low-pressure

© 2024 Wiley-VCH GmbH

16163028, 0, Downloaded from https://onlinelibrary.wiley.com/doi/10.1002/adfm.202404403 by Cas-Beijing Institution Of, Wiley Online Library on [30/06/2024]. See the Terms and Conditions (https://onlinelibrary.wiley.com/terms-and-conditions) on Wiley Online Library for rules of use; OA articles are governed by the applicable Creative Commons License

region (<4 kPa). Whereas, a lower value of 200 mV kPa^{-1} is observed in the high-pressure region (>4 kPa), likely due to the theoretical limits of effective strains in materials under higher pressures. The mixed-dimensional heterostructure significantly enhances responsiveness to tiny stresses by amplifying the deformation of internal piezoelectric NFs. Also, the lightweight nature, lower modulus, and void structures of the nanofibrous membranes promotes shape deformation, further facilitating pressure-electricity responses. The sensitivity is also reflected by the observation that electric responses vary significantly with the imparting frequency (Figure 5e). It is worth noting that the responsivity of our MPHs is superior to that of other reported piezoelectric polymeric systems, for instance, poly(trifluoroethylene) [P(VDF-TrFE)] (410 mV kPa^{-1}),[16] poly(vinylidene fluoride-co-hexafluoropropylene) (PVDF-HFP)/Fe_3O_4 (470 mV kPa^{-1})[27] and PVDF/ZnO (620 mV kPa^{-1})[37] (Figure 5f; Table S4, Supporting Information).[16,27,36–38] Beyond the model polymers utilized in this work, the piezoelectric performance of MPHs could be further enhanced by assembling high-piezoelectricity polymers like PVDF and its copolymers. For instance, MPHs comprising nylon-11/PVDF pair, both intrinsically piezoelectric, can be also fabricated and exhibit higher piezoelectric outputs compared to the nylon-11/PCL combination (Figure S10, Supporting Information). This highlights the remarkable versatility and adaptability of our proposed concept in developing all-organic, high-performance piezoelectric devices.

The outstanding durability and fatigue-resistance were demonstrated through repeated impacting. Significantly, neither performance loss nor structural damage was observed over 6000 cycles of continuous operation, confirming the stability and robustness of the devices (Figure 5g). This excellent durability benefits from the stabilized interlocked nanofibrous structure by the robust 1D/2D mixed-dimensional heterostructure, as discussed earlier. It has also to be mentioned that MPH devices exhibit stable performances over long-term storage, enduring from winter to summer conditions. As shown in Figure 5h, after 6 months of storage, the output performance shows no apparent degradation, indicating the favorable weatherability of MPHs with strongly bonded interfacial interactions between component nanostructures.

2.4. Applications of MPHs for Piezoelectric Sensing

Benefiting from the exceptional lightweight, flexibility and force-sensitive piezoelectricity, MPHs prove ideal for application as self-powered wearable pressure sensors, enabling real-time monitoring of movements under various conditions (**Figure 6a**). A wireless motion monitoring system was developed by integrating the piezoelectric MPH sensor, a WIFI module driven by the power supply of a portable digital oscilloscope, alongside a mobile terminal and customized software. To illustrate its capabilities, the sensor was attached to the knee of an adult cyclist to monitor body movements during cycling (Figure 6b). Real-time motion signals, represented by piezoelectric outputs, were captured and displayed on a mobile phone screen. As the cyclist pedaled along the street, continuous periodic electric signals were displayed, with the time intervals between peaks corresponding to the pedaling frequency. This established a quantitative relationship between pedaling frequency or speed and the electrical signals generated by the MPH sensor (Figure 6c). The recorded motion signals provided precise extraction of specific travel information, including moving distance, speed, and time (Figure 6d–f). The wireless monitoring system, driven by the MPH sensor, plays a critical role in unveiling the "black box" information of human motions toward guiding movements and training athletes.

In addition, owing to the smart responsiveness of MPHs to tiny force changes, the sensor could also simultaneously detect subtle physiological movements such as eye blinking, breathing, and speaking (Figure 6g). The sensor can monitor some subtle physiological motions like eye blinking. As for breathing monitoring, the deeper breath yields higher electric outputs as a result of increased stress deformation exerted on the sensor. Positioned on the throat, the MPH sensor can detect swallowing and speaking movements. The detected motion signals from the throat are perfectly consistent in both frequency and magnitude with the throat movements such as speaking, coughing, and drinking. These observations validate the capability of MPH-based sensors to accurately distinguish human movements. The comprehensive information obtained from the sensor can assist in the clinical diagnosis and disease prevention. The outstanding pressure sensing performances make MPHs promising candidates for daily-life energy harvesting and self-powered monitoring in soft robots, wearable electronics, human-machine interfaces, and other applications. Moreover, the fabrication of MPHs can be easily scaled up to industrial levels by integrating fiber fabrication and ECA process in a single processing line as illustrated in Figure S11 (Supporting Information), facilitating large-scale production and widespread adoption in commercial applications requiring flexible, all-organic piezoelectric materials. Additionally, the freestanding, flexible, and lightweight nature of MPHs makes them highly suitable for integration into wearable devices, energy harvesters, and sensors, further enhancing their commercial viability.

3. Conclusion

In summary, we have successfully fabricated a kind of mixed-dimensional all-organic polymer heterostructures (MPHs) with enhanced piezoelectricity based on model polymers of nylon-11 and PCL using a facile, universal, and scalable strategy. Through epitaxial crystallization-driven assembly, our strategic approach enables controlled growth of MPHs combining polymeric 1D nanofibers and 2D crystals. Simultaneously, this process induces the preferential formation of electroactive crystals, whose molecular mechanism is revealed to be a solvent-induced phase transition through protonation effect. By epitaxially growing 2D polymer crystals on 1D nanofibers, the resulting MPHs exhibit enlarged deformability and dipole polarizations under external stress. The piezoelectricity is highly tunable by modulating morphological evolutions of MPHs. Furthermore, the crosslinking effect of epitaxial 2D crystals on 1D nanofibers via interfacially intermolecular hydrogen-bonding interactions leads to a stabilized interlocked nanofibril network within MPHs, rendering mechanical robustness, stabilization, and flexibility. These advancements culminate in MPH-based devices with exceptional performance in energy harvesting and

© 2024 Wiley-VCH GmbH

16163028, 0, Downloaded from https://onlinelibrary.wiley.com/doi/10.1002/adfm.202404403 by Cas-Beijing Institution Of, Wiley Online Library on [30/06/2024]. See the Terms and Conditions (https://onlinelibrary.wiley.com/terms-and-conditions) on Wiley Online Library for rules of use; OA articles are governed by the applicable Creative Commons License

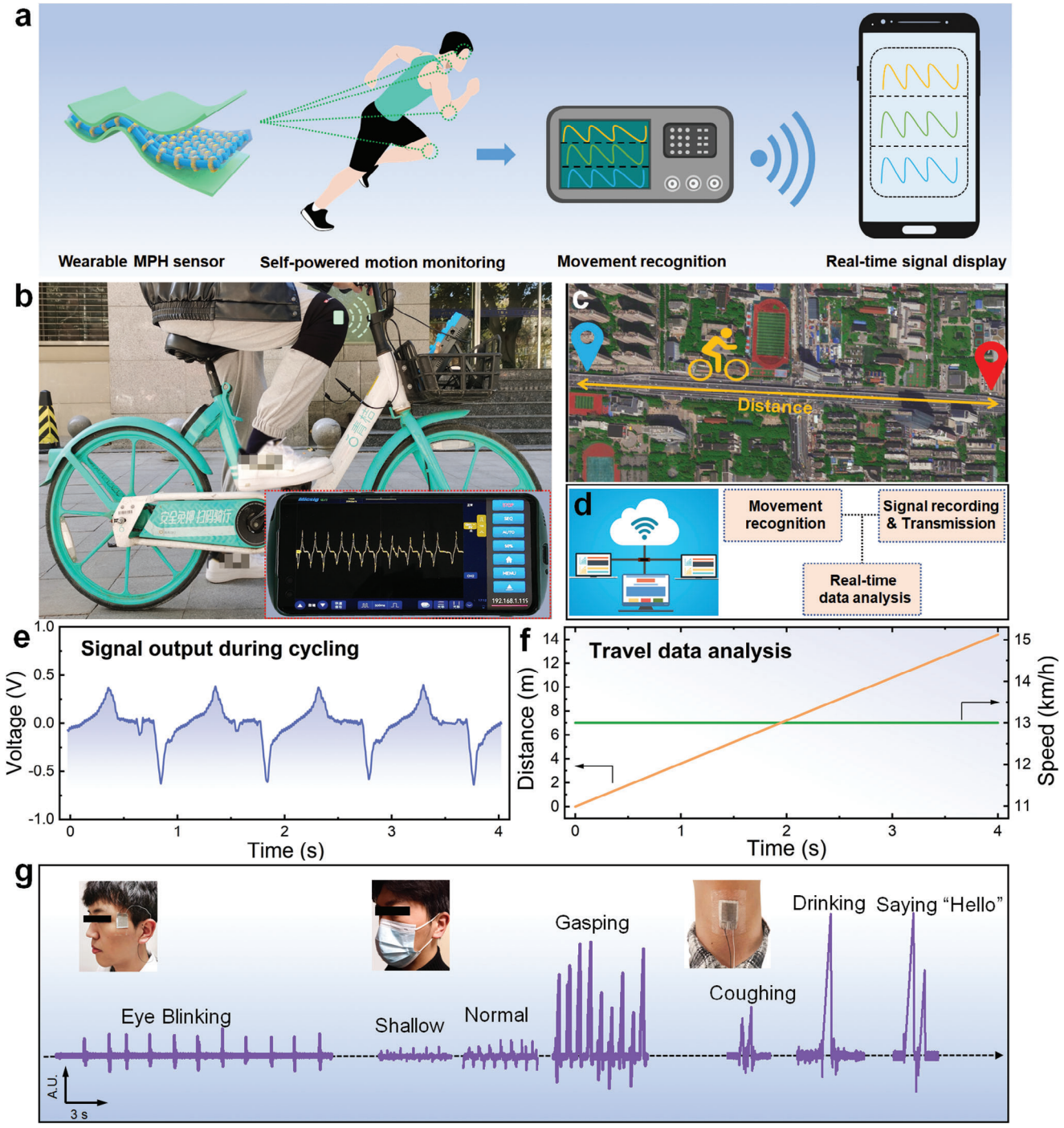

Figure 6. Demonstration of wireless motion monitoring applications based on MPHs. a) Schematic illustration of the wireless human motion monitoring system based on wearable self-powered MPH sensors. b) Photograph of the integrated wearable MPH sensor worn on the knee of cyclist for movement monitoring during cycling. c) Roadmap of cycling for movement monitoring. d) Schematic illustration of the principle for the wireless monitoring system. e) Signal outputs and f) travel data extracted by the MPH sensor during cycling. g) Singal outputs by the sensor under human psychological movements: eye blinking, breathing at different depths, speaking, coughing and drinking.

self-powered wireless detection of subtle physiological motions, demonstrating promising applications in wearable and portable electronics for the electrical Internet of Things. Our versatile mixed-dimensional assembly strategy offers a general toolbox for designing high-performance, all-organic polymeric piezoelectric devices. Looking ahead, we envision extending this concept to more piezoelectric polymers beyond those studied here, thus paving the way for the development of next-generation piezoelectric energy harvesting and self-powered sensing devices.

© 2024 Wiley-VCH GmbH

16163028, 0, Downloaded from https://onlinelibrary.wiley.com/doi/10.1002/adfm.202404403 by Cas-Beijing Institution Of, Wiley Online Library on [30/06/2024]. See the Terms and Conditions (https://onlinelibrary.wiley.com/terms-and-conditions) on Wiley Online Library for rules of use; OA articles are governed by the applicable Creative Commons License

4. Experimental Section

Materials: Nylon-11 (Rilsan BESNO P40 TL) with a weight-average molecular weight M_w of 17.2 kg mol^{-1} was supplied by Arkema, France. PCL (CAPA 6400) with an M_w of 37.0 kg mol^{-1} was purchased from Perstorp, UK. Trifluoroacetic acid (TFA, 99%) and 1,1,1,3,3,3-Hexafluoro-2-propanol (HFIP, 99.5%) were obtained from Shanghai Macklin Biochemical Technology Co., Ltd. Acetic acid (AcOH, analytical grade) was purchased from Tianjin Fuyu Fine Chemical Co., Ltd. All chemicals were utilized without further purifications.

Preparation of Nylon-11 NFs: Nylon-11 NFs were prepared using electrospinning process. The electrospinning solution with a concentration of 5.0 wt% was formulated by dissolving nylon-11 pellets in a mixed solvent of TFA/HFIP (1:1, v/v). During electrospinning, the solution was injected from a syringe at a flow rate of 0.3 mL h^{-1}, under a voltage of 13.0 kV with a spinneret-to-collector distance of 15 cm. Aligned NFs were obtained using a rotating collector at a speed of 2800 rpm.

Preparation of MPHs Based on Model Nylon-11@PCL Hybrids: Mixed-dimensional all-organic polymer heterostructures (MPHs) based on model polymers were prepared through an epitaxial crystallization-driven assembly (ECA). The assembly process occurred in doping polymer solutions at low concentrations around the critical overlap concentration c^*. This threshold, which differentiates the dilute and semidilute concentration regimes, was calculated using the formula:[39]

$$c^* = \frac{3M_w}{4\pi R_g^3 N_A} \tag{3}$$

where N_A is the Avogadro's number, and R_g is the radius of gyration of polymer chains determined by the relation:[40]

$$\left\langle R_g^2 \right\rangle = \frac{C_\infty b^2 N}{6} \tag{4}$$

where C_∞ is the Flory's characteristic ratio (≈4.9 for PCL[41]), N is the degree of polymerization determined by $N = M_w/M_0$ with M_0 being the monomer molar mass (M_0 = 114.15 g mol^{-1} for PCL); b is the Kuhn length that can be estimated by:

$$b = \frac{C_\infty l}{\cos(\frac{\theta}{2})} \tag{5}$$

where l is the C–C bond length (≈1.54 Å) and θ is the bond angle (≈70.5°).[40] The computed critical overlap concentration value for PCL is 0.43 wt%.

In brief, PCL pellets were first dissolved in a mixture of AcOH and deionized water (1:1, v/v) at 70 °C to obtain homogeneous and transparent solutions. The concentration of PCL solutions (c) reported in this study ranged from 0.1 to 5.0 wt% ($0.1 < c/c^* < 10$), covering dilute and semidilute regimes. Afterward, nylon-11 nanofibrous membrane was incubated in PCL/AcOH solution at 25 °C (to ensure adequate supercooling degree around the PCL crystallization temperature T_c = 31 °C, Figure S12, Supporting Information) for 5 min to allow the in-situ growth of PCL crystals on the surface of NFs. As the additional polymer crystals nucleated and grew epitaxially on 1D fibers, the MPH membranes were formed. As-obtained membranes were further dried under vacuum to remove residual solvent. A set of model MPH membranes based on nylon-11@PCL hybrids were prepared by varying the concentration of PCL doping polymer solutions. The resulting MPH membranes were labeled as "MPH-*x*", where "*x*" indicates the concentration of doping PCL solution. For reference, control polymer membranes were also processed under the same conditions.

Characterizations: The morphology of MPH membranes was observed using scanning electron microscopy (SEM, JSM-6380, JEOL) and atomic force microscopy (AFM, MultiMode 8, Bruker). Morphology and chemical compositions of MPHs were characterized by transmission electron microscopy (TEM, FEI Tecnai G2 F20) equipped with energy-dispersive spectroscopy (EDS). Crystallographic structures were characterized by 2D wide-angle X-ray diffraction (WAXD) with an X-ray diffractometer (D8 Discover, Bruker) with CuKα radiation source (λ = 0.154 nm). Intermolecular interactions and crystalline phases were analyzed by Fourier transform infrared spectroscopy (FTIR, Thermo Nicolet 6700). Thermal analyzes were performed using differential scanning calorimetry (DSC, Q2000,TA Instruments) at heating/cooling rates of 10 °C min^{-1} under nitrogen atmosphere. Mechanical properties were evaluated by a universal testing machine (UTM2203, Suns Technology Co., Ltd.) at a crosshead speed of 10 mm min^{-1}. Piezoelectric properties were measured by an electrometer (Keithley 6514) and a portable digital oscilloscope (Micsig STO1102C). Piezoelectric devices with an effective dimension of 3.0 × 3.0 cm^2 were fabricated by sandwiching MPH membranes between two copper-nickel fabric electrodes, followed by encapsulation with polyimide films for protection.

Supporting Information

Supporting Information is available from the Wiley Online Library or from the author.

Acknowledgements

This work was supported by National Key Research and Development Program of China (2019YFA0706800, 2021YFB3200302, and 2021YFB3200304), National Natural Science Foundation of China (52203052, 52125205, U20A20166, and 52192614), China Postdoctoral Science Foundation (2019M650174), and the China 111 project (D18023).

Conflict of Interest

The authors declare no conflict of interest.

Data Availability Statement

The data that support the findings of this study are available from the corresponding author upon reasonable request.

Keywords

all-organic heterostructures, flexible energy harvesters, force-sensitive microstructure, piezoelectric polymers, self-powered devices

Received: April 3, 2024
Published online:

[1] X. Cao, Y. Xiong, J. Sun, X. Zhu, Q. Sun, Z. L. Wang, *Adv. Funct. Mater.* **2021**, *31*, 2102983.
[2] Y.-H. Shin, J. Choi, S. J. Kim, S. Kim, D. Maurya, T.-H. Sung, S. Priya, C.-Y. Kang, H.-C. Song, *Nano Energy* **2020**, *77*, 104986.
[3] J. Kan, W. Liao, J. Wang, S. Wang, M. Yan, Y. Jiang, Z. Zhang, *Nano Energy* **2021**, *89*, 106466.
[4] Z. Li, C. Fei, S. Yang, C. Hou, J. Zhao, Y. Li, C. Zheng, H. Wu, Y. Quan, T. Zhao, D. Chen, D. Li, G. Niu, W. Ren, M. Xiao, Y. Yang, *Adv. Funct. Mater.* **2022**, *32*, 2209173.
[5] K. Dong, X. Peng, Z. L. Wang, *Adv. Mater.* **2020**, *32*, 1902549.
[6] M. Acosta, N. Novak, V. Rojas, S. Patel, R. Vaish, J. Koruza, G. A. Rossetti, J. Rödel, *Appl. Phys. Rev.* **2017**, *4*, 041305.
[7] B. Kumar, S.-W. Kim, *Nano Energy* **2012**, *1*, 342.

© 2024 Wiley-VCH GmbH

16163028, 0, Downloaded from https://onlinelibrary.wiley.com/doi/10.1002/adfm.202404403 by Cas-Beijing Institution Of, Wiley Online Library on [30/06/2024]. See the Terms and Conditions (https://onlinelibrary.wiley.com/terms-and-conditions) on Wiley Online Library for rules of use; OA articles are governed by the applicable Creative Commons License

[8] P. M. Rørvik, T. Grande, M.-A. Einarsrud, *Adv. Mater.* **2011**, *23*, 4007.
[9] F. R. Fan, W. Tang, Z. L. Wang, *Adv. Mater.* **2016**, *28*, 4283.
[10] R. G. Kepler, R. A. Anderson, *Adv. Phys.* **1992**, *41*, 1.
[11] a) J. Sun, H. Guo, J. Ribera, C. Wu, K. Tu, M. Binelli, G. Panzarasa, F. W. M. R. Schwarze, Z. L. Wang, I. Burgert, *ACS Nano* **2020**, *14*, 14665; b) J. Sun, H. Guo, G. N. Schädli, K. Tu, S. Schär, F. W. M. R. Schwarze, G. Panzarasa, J. Ribera, I. Burgert, *Sci. Adv.* **2021**, *7*, eabd9138.
[12] M. Smith, S. Kar-Narayan, *Int. Mater. Rev.* **2022**, *67*, 65.
[13] J. Wu, D. Xiao, J. Zhu, *Chem. Rev.* **2015**, *115*, 2559.
[14] B. Chai, K. Shi, Y. Wang, Y. Liu, F. Liu, P. Jiang, G. Sheng, S. Wang, P. Xu, X. Xu, X. Huang, *Nano Lett.* **2023**, *23*, 1810.
[15] S. Yu, Y. Tai, J. Milam-Guerrero, J. Nam, N. V. Myung, *Nano Energy* **2022**, *97*, 107174.
[16] L. Persano, C. Dagdeviren, Y. Su, Y. Zhang, S. Girardo, D. Pisignano, Y. Huang, J. A. Rogers, *Nat. Commun.* **2013**, *4*, 1633.
[17] M. Baniasadi, Z. Xu, J. Cai, S. Daryadel, M. Quevedo-Lopez, M. Naraghi, M. Minary-Jolandan, *Polymer* **2017**, *127*, 192.
[18] R. A. Surmenev, T. Orlova, R. V. Chernozem, A. A. Ivanova, A. Bartasyte, S. Mathur, M. A. Surmeneva, *Nano Energy* **2019**, *62*, 475.
[19] N. A. Shepelin, A. M. Glushenkov, V. C. Lussini, P. J. Fox, G. W. Dicinoski, J. G. Shapter, A. V. Ellis, *Energy Environ. Sci.* **2019**, *12*, 1143.
[20] A. Datta, Y. S. Choi, E. Chalmers, C. Ou, S. Kar-Narayan, *Adv. Funct. Mater.* **2017**, *27*, 1604262.
[21] K. Eom, S. Na, J.-K. Kim, H. Ko, J. Jin, S. J. Kang, *Nano Energy* **2021**, *88*, 106244.
[22] a) S. R. A. Ruth, V. R. Feig, H. Tran, Z. Bao, *Adv. Funct. Mater.* **2020**, *30*, 2003491; b) Y.-S. Kim, Y. Xie, X. Wen, S. Wang, S. J. Kim, H.-K. Song, Z. L. Wang, *Nano Energy* **2015**, *14*, 77; c) M. M. Abolhasani, M. Naebe, M. Hassanpour Amiri, K. Shirvanimoghaddam, S. Anwar, J. J. Michels, K. Asadi, *Adv. Sci.* **2020**, *7*, 2000517.
[23] C. Wan, C. R. Bowen, *J. Mater. Chem. A* **2017**, *5*, 3091.
[24] Z. Wang, R. Yu, C. Pan, Y. Liu, Y. Ding, Z. L. Wang, *Adv. Mater.* **2015**, *27*, 1553.
[25] J.-H. Zhang, Z. Li, J. Xu, J. Li, K. Yan, W. Cheng, M. Xin, T. Zhu, J. Du, S. Chen, X. An, Z. Zhou, L. Cheng, S. Ying, J. Zhang, X. Gao, Q. Zhang, X. Jia, Y. Shi, L. Pan, *Nat. Commun.* **2022**, *13*, 5839.
[26] X. Chen, X. Li, J. Shao, N. An, H. Tian, C. Wang, T. Han, L. Wang, B. Lu, *Small* **2017**, *13*, 1604245.
[27] H. Li, W. Lian, T. Cheng, W. Zhang, B. Lu, K. Tan, C. Liu, C. Shen, *ACS Sustainable Chem. Eng.* **2021**, *9*, 17128.
[28] T. Li, M. Qu, C. Carlos, L. Gu, F. Jin, T. Yuan, X. Wu, J. Xiao, T. Wang, W. Dong, X. Wang, Z.-Q. Feng, *Adv. Mater.* **2021**, *33*, 2006093.
[29] a) S. Anwar, D. Pinkal, W. Zajaczkowski, P. von Tiedemann, H. Sharifi Dehsari, M. Kumar, T. Lenz, U. Kemmer-Jonas, W. Pisula, M. Wagner, R. Graf, H. Frey, K. Asadi, *Sci. Adv.* **2019**, *5*, eaav3489; b) Y. M. Yousry, K. Yao, A. M. Mohamed, W. H. Liew, S. Chen, S. Ramakrishna, *Adv. Funct. Mater.* **2020**, *30*, 1910592.
[30] a) Z. Zhang, M. H. Litt, L. Zhu, *Macromolecules* **2016**, *49*, 3070; b) M. A. Woodruff, D. W. Hutmacher, *Prog. Polym. Sci.* **2010**, *35*, 1217.
[31] B. Wunderlich, *Macromolecular Physics. Vol. 2: Crystal Nucleation, Growth, Annealing*, Academic Press, New York **1976**.
[32] S. S. Nair, C. Ramesh, K. Tashiro, *Macromolecules* **2006**, *39*, 2841.
[33] a) Y. S. Choi, S. K. Kim, F. Williams, Y. Calahorra, J. A. Elliott, S. Kar-Narayan, *Chem. Commun.* **2018**, *54*, 6863; b) S. Anwar, M. Hassanpour Amiri, S. Jiang, M. M. Abolhasani, P. R. F. Rocha, K. Asadi, *Adv. Funct. Mater.* **2021**, *31*, 2004326.
[34] S. M. Aharoni, *N-Nylons: Their Synthesis, Structure, and Properties*, Wiley, New York **1997**.
[35] J. R. Schaefgen, C. F. Trivisonno, *J. Am. Chem. Soc.* **1951**, *73*, 4580.
[36] Y. Guan, L. Tu, K. Ren, X. Kang, Y. Tian, W. Deng, P. Yu, C. Ning, R. Fu, G. Tan, L. Zhou, *ACS Appl. Mater. Interfaces* **2023**, *15*, 1736.
[37] Y. Tan, K. Yang, B. Wang, H. Li, L. Wang, C. Wang, *Nano Res.* **2021**, *14*, 3969.
[38] a) J. Lu, S. Hu, W. Li, X. Wang, X. Mo, X. Gong, H. Liu, W. Luo, W. Dong, C. Sima, Y. Wang, G. Yang, J.-T. Luo, S. Jiang, Z. Shi, G. Zhang, *ACS Nano* **2022**, *16*, 3744; b) D.-N. Nguyen, W. Moon, *J. Appl. Polym. Sci.* **2020**, *137*, 48884; c) S. Ye, C. Cheng, X. Chen, X. Chen, J. Shao, J. Zhang, H. Hu, H. Tian, X. Li, L. Ma, W. Jia, *Nano Energy* **2019**, *60*, 701; d) C. Yan, W. Deng, L. Jin, T. Yang, Z. Wang, X. Chu, H. Su, J. Chen, W. Yang, *ACS Appl. Mater. Interfaces* **2018**, *10*, 41070; e) J. J. Wei, L. K. Yan, J. L. Song, M. Chao, *Russ. J. Appl. Chem.* **2015**, *88*, 2029; f) G. Wu, O. Yano, T. Soen, *Polym. J.* **1986**, *18*, 51; g) R. Li, Z. Shi, D. Kuang, J. Pei, *Int. J. Polym. Sci.* **2016**, *2016*, 1; h) B. A. Newman, K. G. Kim, J. I. Scheinbeim, *J. Mater. Sci.* **1990**, *25*, 1779; i) S. Liu, Z. Cui, P. Fu, M. Liu, Y. Zhang, R. Jia, Q. Zhao, *Appl. Phys. Lett.* **2014**, *104*, 172906; j) E. S. Choi, H. C. Kim, R. M. Muthoka, P. S. Panicker, D. O. Agumba, J. Kim, *Compos. Sci. Technol.* **2021**, *209*, 108795; k) M. Ando, D. Tamakura, T. Inoue, K. Takumi, T. Yamanaga, R. Todo, K. Hosoya, O. Onishi, *Jpn. J. Appl. Phys.* **2019**, *58*, SLLD09.
[39] a) Q. Ying, B. Chu, *Macromolecules* **1987**, *20*, 362; b) C. Clasen, J. P. Plog, W. M. Kulicke, M. Owens, C. Macosko, L. E. Scriven, M. Verani, G. H. McKinley, *J. Rheol.* **2006**, *50*, 849.
[40] M. Rubinstein, R. H. Colby, *Polymer Physics*, Oxford University Press, Oxford **2003**.
[41] L. Yuan, N. Hamidi, S. Smith, F. Clemons, A. Hamidi, C. Tang, *Eur. Polym. J.* **2015**, *62*, 43.

© 2024 Wiley-VCH GmbH

16163028, 0, Downloaded from https://onlinelibrary.wiley.com/doi/10.1002/adfm.202404403 by Cas-Beijing Institution Of, Wiley Online Library on [30/06/2024]. See the Terms and Conditions (https://onlinelibrary.wiley.com/terms-and-conditions) on Wiley Online Library for rules of use; OA articles are governed by the applicable Creative Commons License